Mode Coupling in Dynamic Atomic Force Microscopy

Mode coupling in Dynamic Atomic Force Microscopy

Abhilash Chandrashekar,[1,*] Pierpaolo Belardinelli,[2] Stefano Lenci,[2] Urs Staufer,[1] and Farbod Alijani[1,†]

[1]*Precision and Microsystems Engineering, TU Delft, Delft, The Netherlands*
[2]*DICEA, Polytechnic University of Marche, Ancona, Italy*

(Dated: December 17, 2020)

Enhancing the signal-to-noise ratio in dynamic Atomic Force Microscopy (AFM) plays a key role in nanomechanical mapping of materials with atomic resolution. In this work, we develop an experimental procedure for boosting the sensitivity of higher harmonics of an AFM cantilever without modifying the cantilever geometry but instead by utilizing dynamical mode coupling between its flexural modes of vibration. We perform experiments on different cantilevers and samples and observe that via nonlinear resonance frequency tuning, we can obtain a frequency range where strong modal interactions lead up to 7 and 16 folds increase in the sensitivity of the 6^{th} and 17^{th} harmonic while reducing sample indentation. We derive a numerical model that captures the observed physics and confirms that nonlinear mode coupling can be held accountable for increasing the amplitude of higher harmonics during tip-sample interactions.

I. INTRODUCTION

Dynamic Atomic Force Microscopy (AFM) has emerged as a powerful tool for nanoscale imaging of matter in many technical and scientific application areas [1]. In dynamic AFM, an oscillating microcantilever tip interacts intermittently with the sample while being driven close to or at a resonance frequency. Dynamic AFM is routinely used to characterize the topography of samples with nanometer or even atomic resolution. Irrespective of the outstanding capabilities offered by this AFM mode, the understanding of nanoscale processes and quantification of material properties using AFM is yet far from being well-established. One curbing reason for this is that, in the conventional dynamic AFM experiments a single drive frequency is used to scan the sample and the feedback system maintains either the amplitude or the phase of oscillations constant. As a result, the number of observable channels that are required to quantify the mechanical properties of the sample are not sufficient. To overcome this limitation, multi-frequency AFM techniques are being adopted [2]. These methods mainly use higher harmonics of the cantilever deflection signal [3, 4] or the output signals of two or three resonant modes [5, 6] to obtain complementary information of the interacting sample. Other modes of multi-frequency AFM are also available that use torsional harmonics [7] or intermodulation products [8] to probe sample properties.

To date, many studies have incorporated the aforementioned multi-frequency AFM techniques to map nanomechanical properties of samples, ranging from polymeric [9, 10] to biological substances[11, 12]. However, only a handful of these works have looked into the possibilities for enhancing the sensitivity of the higher order spectral components [13–17]. Among them, a majority have exploited a phenomenon known as internal resonance [18]. This condition occurs when the ratio between two or more resonance frequencies of the cantilever is a rational number, and results in strong coupling between the interacting modes of vibration [19]. The significance of intermodal coupling arises from its correlation with the effective spring constant of the resonant modes that can be tuned either by modifying the geometry of the cantilever [13, 15], or creating notches/ holes [16], or by adding concentrated mass at specific locations on the cantilever [17].

Here, in contrast to previous works, we propose a novel technique to boost the signal-to-noise ratio (SNR) of higher harmonics and higher order flexural mode of an AFM cantilever without the need to modify its geometry. By sweeping the drive frequency in the spectral neighborhood of a resonance, we find a frequency range where strong interactions between the first three flexural modes of the cantilever significantly increases the amplitude of higher harmonics. Using this technique, we are able to enhance the amplitude of the 6^{th} and the 17^{th} harmonic up to 7 and 16 folds, respectively. Interestingly, driving the cantilever in this frequency range also results in a decreased sample indentation due to the phase synchronization of the eigenmodes. These phenomena are showcased at drive amplitudes comparable to set point ratios used in conventional scanning operation, thereby highlighting the utility of the technique in dynamic AFM. To understand the physics behind our observations, we develop a theoretical model comprising Multiple-Degrees of Freedom (MDOF) and non-smooth nonlinear interactions between the tip and the sample. Our simulations qualitatively conform with the observed physics, and confirms that mode coupling is responsible for the increase in the SNR of higher harmonics. Our study also reveals the use of real-time temporal data for identifying dynamical coupling in AFM applications. Because of its simplicity and ease of use, the proposed technique has the potential to be utilised in a variety of multi-frequency AFM techniques.

II. EXPERIMENTAL RESULTS

Our experiments are performed by using a commercial AFM (JPK Nanowizard) and two separate acquisition electronics, namely a multi-lock-in amplifier from Intermodulation products and a Field Programmable Gated Array (FPGA) from National Instruments, to collect and analyze the can-

* a.chandrashekar@tudelft.nl
† f.alijani@tudelft.nl

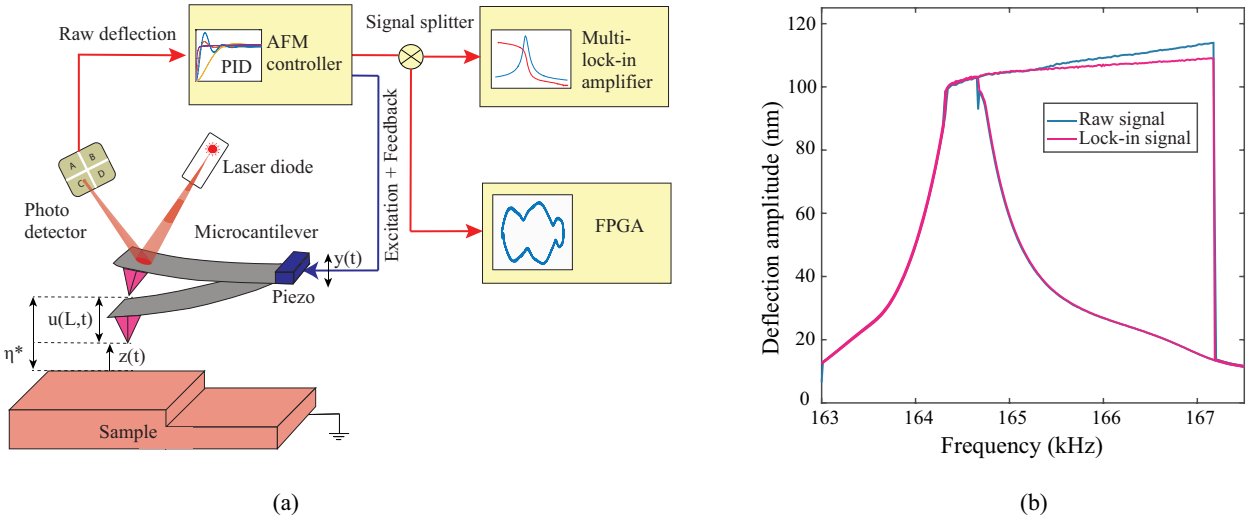

FIG. 1: Schematic of the experimental setup and the acquired experimental nonlinear dynamic response. The response is obtained with a commercial rectangular cantilever (NCLR) on a Silicon sample with an excitation amplitude of 0.013 V. (a) The schematic of the setup employing two different data acquisition electronics, namely the multi-lock-in amplifier and an FPGA device. The schematic details the initial static cantilever configuration η^* and the dynamic configuration with the cantilever vibrating about the elastostatic equilibrium u at the free end L of the cantilever. (b) The blue and the pink curves indicate the nonlinear dynamic response obtained using the raw deflection signal and the lock-in signal. The forward and reverse sweeps are combined into one curve.

tilever deflection data. We used a commercially available rectangular Silicon cantilever (NCLR, NanoWorld AG) and a flat Silicon sample to perform the experiments. For each experiment, the spring constant of the cantilever (k = 22.68 N m^{-1}), its resonance frequency (f_0 = 164.52 kHz), and quality factor (Q = 428) are determined using the thermal calibration method [20]. A schematic of the setup is shown in Fig. 1(a).

In order to obtain the nonlinear resonance response of the AFM cantilever while interacting with the sample, we have implemented a procedure where a standard force-distance curve is first used to statically approach the sample surface with a small set point of 2 nm. Next, the end condition of the force-distance curve is preserved to hold the cantilever at the precise fixed distance of η^* =100 nm from the sample surface. The latter operation is feasible using the feedback loop on the z-piezo of the AFM, which stays active for a specific period of time. While maintaining the static position (η^*), the drive frequency (f_d) of the dither piezo is swept around the resonance frequency from 163 kHz to 170 kHz (f_0=164.52 kHz). The resulting change in vibrational amplitude is recorded using the multi-lock-in amplifier and the FPGA, simultaneously. Additionally, during the entire sweep duration a specific excitation $y(t)$ is applied such that the reduction in vibrational amplitude due to tip-sample interaction is maintained at 84%. This reduction is comparable with that of the amplitude set-point ratios used during normal scanning operation in dynamic AFM (See Fig. S1.1 in supplementary information S1). The outcome of this procedure is shown in Fig. 1(b). It can be seen that, when the deflection amplitude is increased, the resonance curve first slightly bends to the left (spring softening) [21] and as the tip further approaches the sample, the curve bends towards the right side of the resonance (spring hardening). We note that the presence of nonlinear attractive and repulsive forces between the tip and the sample lie at the root of our observation [22].

In Fig. 1(b) we also observe that the nonlinear resonance curve obtained by using the lock-in amplifier (pink curve) is different from the one obtained by analyzing the raw deflection signal using the FPGA (blue curve). Interestingly, we observe a mismatch in the amplitudes of the two signals that exacerbates at higher f_d. The observed discrepancy hints at the presence of higher-order spectral components that are essentially eliminated when the lock-in amplifier is used. This is because, the lock-in amplifier allows detection of a single frequency component when sweeping f_d around resonance and effectively approximates the cantilever dynamics as a Single-Degree of Freedom (SDOF) system. However, the FPGA stores the real-time deflection signal and thus can efficiently capture modal interactions that may exist around the resonance.

To further investigate the cantilever's nonlinear dynamic response, we obtain the maximum and minimum of the deflection in an oscillatory cycle using the FPGA (see Fig. 2 (a)). We note that the cantilever deflection signal reaches a maximum far away from the sample, whereas the minimum shows that the tip is interacting with the sample. This segregation reveals a broken symmetry in the response due to the non-smooth nature of the contact between the tip and the sample when f_d is detuned from f_0. To study the physical origin of this symmetry breaking response, we trace the phase space trajectories of the cantilever in real-time when moving from f_d = 164.5 kHz to f_d = 167 kHz (see Fig. 2(b)

and (c)). The phase space trajectories are highly sensitive to the presence of higher order modes and can be used to identify modal interactions [22]. In Fig. 2(b) we observe simple harmonic oscillations of the cantilever close to the free air resonance (f_d = 164.5 kHz); however, at large detuning ($f_d \geq$ 166.4 kHz), the phase space warps and ripples appear on the periphery of the trajectory (Fig. 2(c)). To understand the origin of this phase space distortion, we perform Fast Fourier Transform (FFT) of the temporal data (See Fig. 2(d) and (e)), and observe that the frequency content of the signal at f_d=164.5 kHz involves only f_0 and few of its higher harmonics. But, when applying FFT on the time signal taken at f_d=167 kHz, an additional resonance peak appears at f_2 =1020 kHz (see Fig. 2(e)), suggesting the activation of the second eigenmode of the cantilever. In essence, this shows that the phase space distortions are a direct result of activation of higher order vibration modes and that the presence of higher harmonics has trivial effect on these trajectories (see Fig . A.1 of Appendix A for details).

To elaborate on our observation, we note that for the cantilever used in the experiments, the frequency ratio $f_2/f_0 \approx 6.2$ is close to the factor 6. Therefore, by tuning the nonlinear resonance frequency (via sweeping f_d), we can reach a 6:1 internal resonance in the frequency range $f_d \in [165, 166]$ kHz, where the contribution of the second mode becomes apparent. The resulting mode coupling enhances the SNR of specific harmonics that are close to the interacting eigenmode. In particular, we observe a 7 fold increase in the SNR of the 6$^{\text{th}}$ harmonic compared to its amplitude near the free air resonance (refer to Fig. 2(d) and (e)).

Interestingly, this modal interaction is not only characterized by an increase in the strength of harmonics, but it is also accompanied by a reduced sample indentation when compared to normal scanning operations with similar amplitude set-point ratios at $f_d = f_0$. As we sweep f_d around resonance we observe a decrease in the minimum amplitudes in the frequency range between $165 < f_d < 166$ kHz which is associated with a decrease in the sample indentation. Such properties make the frequency range over which mode coupling occurs, an ideal range of excitation for the mapping of nanomechanical properties. Therefore, we label this region as the "sweet spot". This lower sample indentation is highlighted in the inset of Fig. 2(a), and can be formally described as a gradual curving of the nonlinear dynamic curve in its deflection minima forming a convex shape. It may be intuitively thought that the increased coupling should increase the interaction force and, as a consequence, increase the sample indentation. However, in the sweet spot, the phases of the interacting modes synchronize in such a way that there is a reduced sample indentation (See Fig. C 1 in Appendix). This dynamic feature is similar to what has been previously reported in dynamically tuned trapezoidal cantilevers [15].

To investigate the repeatability of the observed phenomena, we performed additional set of experiments using a TAP190Al-G rectangular cantilever on a Highly Oriented Pyrolytic Graphite (HOPG) sample, a TAP300Al-G rectangular cantilever on a nanocrystalline diamond island and finally a TAP150AL-G rectangular cantilever on a Polystyrene island. We found that the "sweet spot" is not a unique feature that belongs to a particular sample-cantilever configuration (see section B of supplementary information S1 for details). These interesting observations highlight the role of higher eigenmodes and mode coupling in AFM applications.

III. MODELING AND SIMULATIONS

In order to underpin the physics behind our experimental observation and to further understand the nature of the mode coupling, we develop a theoretical model based on a non-smooth two-degree of freedom system. The derivation of the model can be found in Appendix B.The model utilizes the long range nonlinear Van der Waals (VdW) and Derjaguin–Muller–Toporov (DMT) contact forces to describe the tip-sample interactions $F_{ts}(z)$ as follows [23, 24]

$$F_{ts}(z) = \begin{cases} F_{\text{vdW}} = -\dfrac{HR}{6z^2} & \text{for } z > a_0 \\ F_{\text{DMT}} = -\dfrac{HR}{6{a_0}^2} + \dfrac{4}{3}E^*\sqrt{R}\,(a_0 - z)^{3/2} & \text{for } z \leq a_0. \end{cases} \tag{1}$$

Here, H stands for the Hamaker constant, R the tip radius, a_0 the intermolecular distance, and E^* the effective Young's modulus. The tip-surface interaction is purely attractive (F_{vdW}) when the separation distance z is larger than the intermolecular distance a_0. If z is smaller than a_0 the interaction is governed by contact mechanics (F_{DMT}). This non-smoothness in the interaction force mediates an energy channel between different modes of the cantilever and acts as the root cause of our observation.

To obtain the equations of motion, we model the AFM cantilever as a continuous dynamical system using the Euler-Bernoulli beam theory. We discretize the model by projecting the cantilever deflection onto its linear eigenmodes (computed near free air resonance) and employ the Galerkin approach to obtain a system of ordinary differential equations as follows [22]

$$\ddot{\tilde{q}}_i + D_i(\bar{z})\,\dot{\tilde{q}}_i + K_i\tilde{q}_i = -C_i - F_{ts,i}(\bar{z}) + B_i\bar{\Omega}^2\bar{y}\sin\left(\bar{\Omega}\tau\right). \tag{2}$$

The cantilever deflection, splitted across the generalized coordinates $\tilde{q}_i$ ($i = 1, 2, ...N$, with N being the number of generalized coordinates), is written in Eq. (2) on a reference system attached to the cantilever (See Fig. 1(a)). The coupling between the generalized coordinates occurs through the relation, $\bar{z} = 1 - \sum_{i=1}^{n} \tilde{q}_i - \bar{y}\sin\bar{\Omega}\tau$. In addition, equation (2) is made dimensionless with respect to the equilibrium gap width (η^*) and the fundamental frequency of the cantilever ($\omega_0 = 2\pi f_0$) in the absence of the tip-sample interaction. The amplitude of the dither piezo is given by $\bar{y}$ and the dotted quantities represent derivatives with respect to the rescaled time τ ($\tau = \omega_0 t$). Additionally, modal damping $D_i(\bar{z})$ has been explicitly added to Eq. (2). In particular, we consider a piecewise model [23] that accounts for the dissipation mechanism when the tip is in

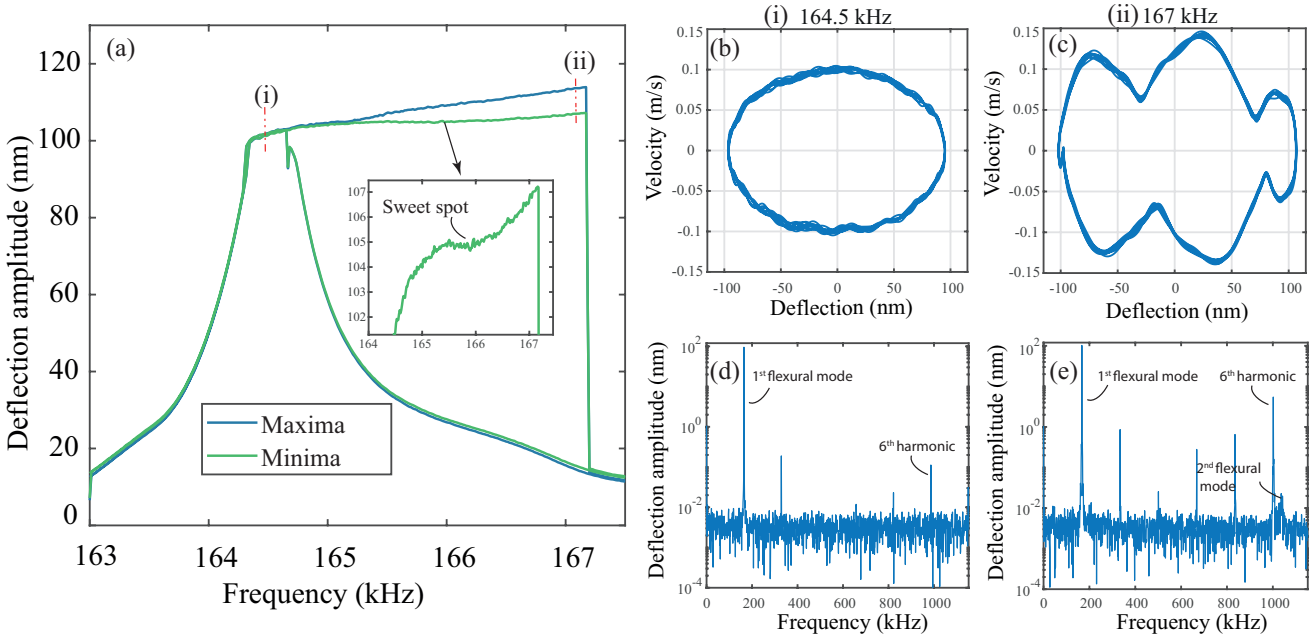

FIG. 2: Experimental nonlinear dynamic response, phase space trajectories and the associated frequency spectra obtained from the raw deflection signal of the cantilever. (a) Experimental frequency response curve; the blue and green curves represent the maximum and minimum position of the tip, respectively. The forward and reverse sweeps are combined into one curve. The inset highlights the gradual curving of the nonlinear dynamic response in a specific range of drive frequency. The sweet spot frequency range is highlighted using dashed lines. (b)-(c) Phase space trajectories at 164.5 kHz and 167 kHz of drive frequency showing the influence of the second eigenmode in the cantilever oscillations. (d)-(e) Frequency spectra of raw deflection signal at 164.5 kHz and 167 kHz showing the presence of higher harmonics and the second eigenmode.

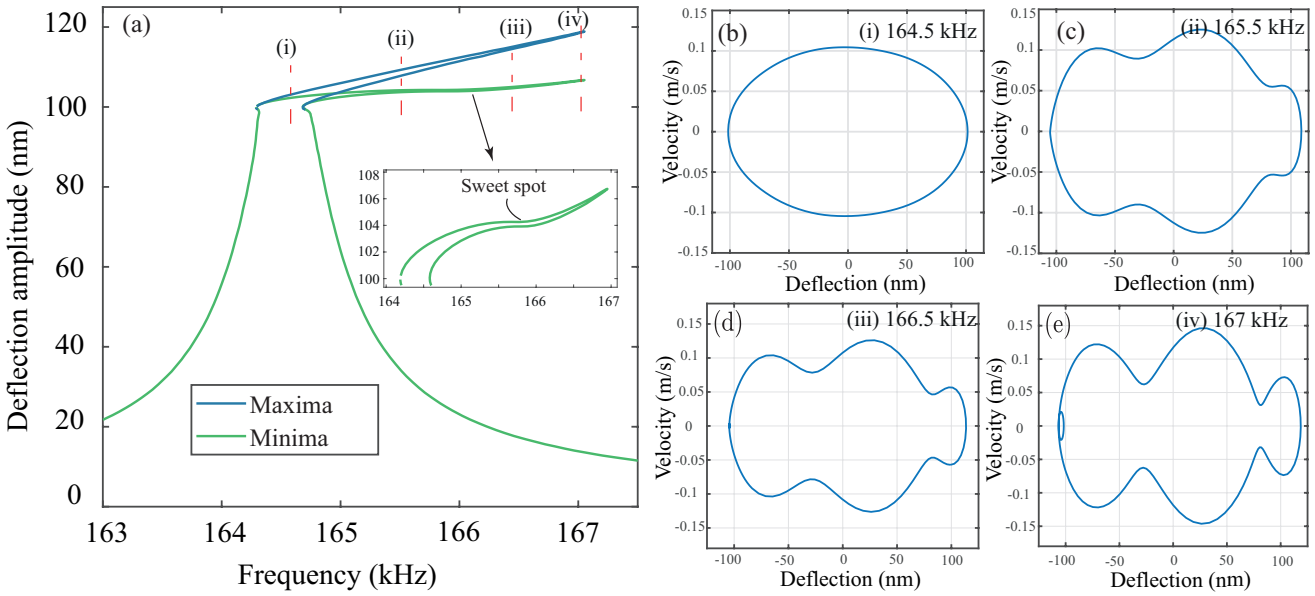

FIG. 3: Simulated nonlinear dynamic response and phase space trajectories obtained using the two mode model. (a) Numerical frequency response curve; the blue and green curves represent the maximum and minimum position of the tip, respectively. The forward and reverse sweeps are combined into one curve. The nonlinear dynamic response is simulated considering 6:1 internal resonance condition between the first two flexural modes. The inset highlights the gradual curving of the nonlinear dynamic response in a specific range of drive frequency. The sweet spot frequency range is highlighted using dashed lines. (b)-(e) Phase space trajectories at 164.5 kHz, 165.5 kHz, 166.5 kHz, and 167 kHz of drive frequency, respectively.

air ($\tilde{D}_i^{\text{att}}$) or when it is in contact with the sample ($\tilde{D}_i^{\text{rep}}$). Finally, the coefficients K_i, C_i, and B_i represent the modal stiff-

ness, static deflection, and mode participation factor, respectively. The final discretized equation is then simulated using pseudo arc-length continuation technique to fit the experimental data [25].

The simulations performed using the two-mode VdW-DMT model qualitatively describe our experimental observations. In Fig. 3(a) the blue and green nonlinear dynamic response curves represent the maximum and minimum deflection of the cantilever similar to what is observed in experiments. Referring to Fig. 3(a), the gradual curving of the minimum response (green curve) occurs when the simulation parameters of the coupled oscillator system are tuned to produce a 6:1 internal resonance condition, confirming the presence of this unconventional internal resonance at a few kHz of detuning (see section C of supplementary information S1 for details) . Adding to this, the theoretical nonlinear dynamic curves highlight the influence of the higher order modes in the distortion of the phase space trajectory. Similar to the experimental results, the periodic orbit exhibits simple harmonic motion close to free air resonance (Fig. 3(b)), which becomes distorted by detuning f_d to higher frequencies. The distortion gradually increases in depth, in accordance with the contribution given by the second mode of vibration (Figs. 3(c)-(e)).

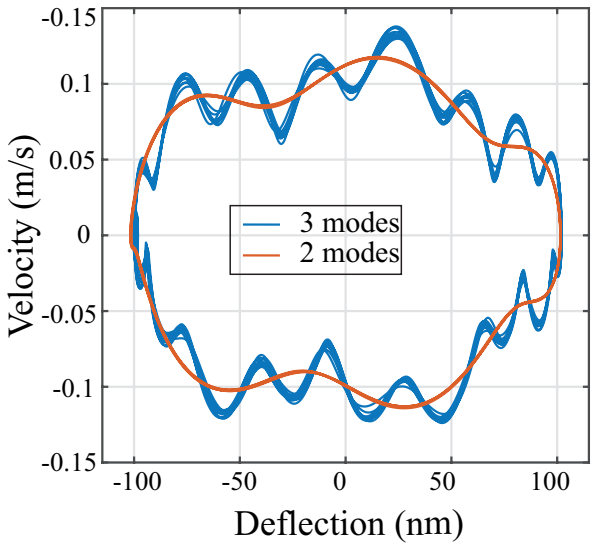

FIG. 4: Phase space trajectories obtained from experimental deflection at f_d= 165.5 kHz. The experimental deflection signal is low pass filtered with different cut off frequencies to identify the contribution from the second (orange curve) and the third flexural mode (blue curve), respectively.

Although the two-mode model accurately predicts the dominance of the second mode at large detunings and explains the physics behind the curving of the nonlinear dynamic response in the sweet spot, it masks the effect of any further couplings that may exist among higher modes of vibration. In particular as depicted in Fig. 4, at f_d = 165.5 kHz we observe an increase in the number of ripples on the periphery of the phase space (blue curve). We note that this additional distortion of the phase space is accompanied with 16 folds increase

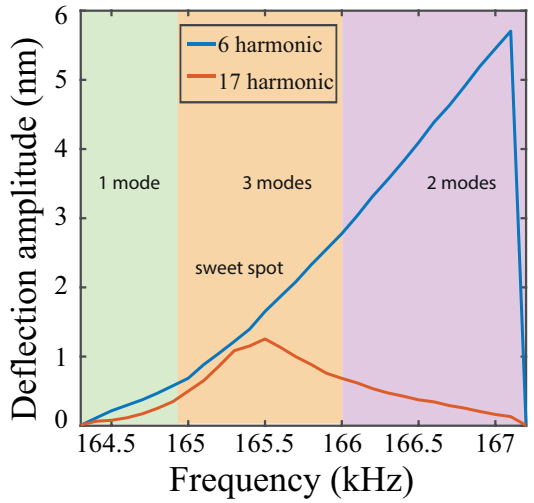

FIG. 5: Variation of the 6th and the 17th harmonic amplitude as a function of the driving frequency f_d. The amplitude of the 6th and the 17th harmonic increase in a specific frequency range highlighted by the orange section due to intermodal coupling. Thereafter, only the 6th harmonic amplitude increases due to increased tip-sample interaction and dominance of the second mode of vibration.

in the amplitude of the 17th harmonic that is closely located to the third flexural mode of the cantilever ($f_3 \approx 17.5 f_0$). To prove our hypothesis about the influence of the third flexural mode, we low-pass filter the experimental data up to the 16th harmonic and observe that the resulting phase space (orange curve) closely matches with that of the simulated trajectory obtained using the two mode approximation model shown in Fig. 3(c). Although including an additional mode in the numerical model (with consequent increase of the complexity in the simulations) could capture completely the dynamics observed in experiments, it would not add physical insights for the observations stated in this article.

Finally, as an extensive outlook on the various stages of influence of higher-order modes as f_d is detuned from f_0, we report in Fig. 5 the variation of the 6th and 17th harmonic as a function of f_d. At first, when f_d is close to f_0, the amplitude of the harmonics generated due to tip-sample forces is relatively low and comparable with the strength of the signals observed during normal tapping mode scanning operation. In the low frequency range (green region of Fig. 5) the entire cantilever dynamics can be well approximated as a SDOF system. With increased detuning, when f_d lies in the sweet spot (orange region), there is sharp increase in the contribution of the second and third eigenmode in the cantilever motion and the dynamics is governed by the three flexural modes of the cantilever. In this region the amplitude of the 6th and 17th harmonic increase by 7 and 16 folds respectively as a consequence of an enhanced mode coupling both with the second and the third eigenmode. Upon further detuning, we observe the continuous increase of SNR of the 6th harmonic but at the expense of an increased sample indentation. At the same time, the large resonance frequency tuning brings the amplitude of the 17th

harmonic to drop gradually, until the third mode contribution completely disappears. In the violet region of Fig. 5, the dynamics is fully governed by the first and the second mode only. Additionally, by increasing the amplitude of the excitation, the sweet spot widens by few kHz while the physics remains unaltered. However, this increase in the sweet spot range comes at the expense of larger set point ratio (see Fig. S1.5 of supplementary information S1 for details).

Currently, the methodology provides significant improvement in SNR of higher harmonics for single point measurements and could be implemented in techniques that extract the nanomechanical properties of samples at several predetermined pixels. However, in order to integrate the technique with conventional scanning operation there are a few limitations that still need to be addressed. In particular, as a first step, the algorithm routine used to capture the raw deflection signal and tune nonlinear resonance frequency has to be integrated into the AFM's controller in order to handle the data processing at imaging speeds. Such integration also helps tackling the issue of choosing the right drive frequency within the sweet spot for samples comprising multiple materials. Secondly, since the sweet spot is driven beyond the bifurcation point into a bi-stable region , a thorough study has to be performed to understand the influence of noise and feedback settings on the robustness of sweet spot during imaging [26, 27]. In this aspect, our technique can be incorporated together with novel feedback architectures such as modulated time delay control [29] that have already been successfully used to control the cantilever oscillations in the bi-stable regime and reduce perturbation-induced jumps during the scanning operation. Finally, it is important to consider the influence of the geometric and modal characteristics of the cantilever used for performing the measurements. The technique reported in this article has been showcased with standard rectangular cantilevers and is applicable to cantilevers with the second and the third bending modes close to $6f_0$ and $17f_0$, respectively.

IV. CONCLUSION

In summary, we propose a technique to actively tune the nonlinear resonance frequency of AFM cantilevers to achieve high SNR of harmonics at low sample indentation compared to conventional dynamic AFM operations. We discuss the influence of higher order modes on the phase space trajectories of the cantilever as a function of the detuned frequency and highlight the presence of a sweet spot in a specific frequency range around resonance where there is a significant increase in the amplitude of higher harmonics, due to strong modal interactions. We use a two mode nonlinear non-smooth model to qualitatively describe our experiments and explain the observed physics. The model reinforces the idea of mode coupling as the phenomenon behind the increase in the amplitude of higher harmonics and the lower sample indentation. Finally, given the ease of use and utility, we anticipate that this experimental technique can be used together with various multi-frequency AFM techniques to study nanomechanical properties of organic and inorganic samples without the need for specialized cantilevers. Our technique can also be easily employed in multi-frequency scanning operations to obtain images of the higher harmonics with increased sensitivity, which is an essential requirement in dynamic AFM applications.

V. ACKNOWLEDGEMENT

This work is part of the research programme 'A NICE TIP TAP' with grant number 15450 which is financed by the Netherlands Organisation for Scientific Research (NWO). The authors also acknowledge fruitful discussions with Dr. Oriel Shoshani about internal resonance, Dr. Gerard Verbiest regarding the experiments, Dr. Daniel Forchheimer for FPGA coding, and Dr. André F. Sartori with sample preparation.

Data availability. The authors declare that all the data in this manuscript are available upon request.

APPENDIX

Appendix A: Influence of harmonics on phase space trajectories

In this section, we study the influence of harmonics and higher order modes on the phase space trajectories and present additional results to corroborate our findings. In particular, we focus on the warping of the phase space trajectories and its insensitivity towards higher harmonics. Figure.A.1 shows the experimental phase space trajectories and the associated frequency spectra at several distinct excitation frequencies. The data is extracted from the nonlinear frequency response curve Fig. 2 (a). The time data is digitally low pass filtered at different stages with different cut off frequencies to understand the influence of higher order spectral components. At first, we choose a frequency point close to the resonance at f_d = 164.4 kHz and obtain the phase space and the corresponding frequency spectra as shown in Fig. A.1(a) and (b). The data is digitally low pass filtered with a cut off frequency of 3.5 MHz. Looking at Fig. A.1 (a), the frequency spectra clearly shows the presence of several higher harmonics and in particular the 6^{th} and the 17^{th} harmonics are of special interest since they are closer to the second and third flexural modes of the cantilever and thus show more contrast in AFM imaging operations. Referring to these figures, even when the higher harmonics are present in the cantilever deflection, the phase space trajectories remain approximately circular and show no signs of warping (see Fig. A.1(b)).

In the next step of the analysis, we choose the frequency point f_d = 165.5 kHz reported in Fig. 4 but low pass filter the time data with two different cut off frequencies namely 1.1 MHz (upto the 7^{th} harmonic) (Fig. A.1(c)-(d)) and 2.65 MHz (upto the 16^{th} harmonic) (Fig.A.1(e)-(f)), respectively. From the frequency spectra of Fig. A.1(c), we see that by including spectral components only until the second mode, we see a

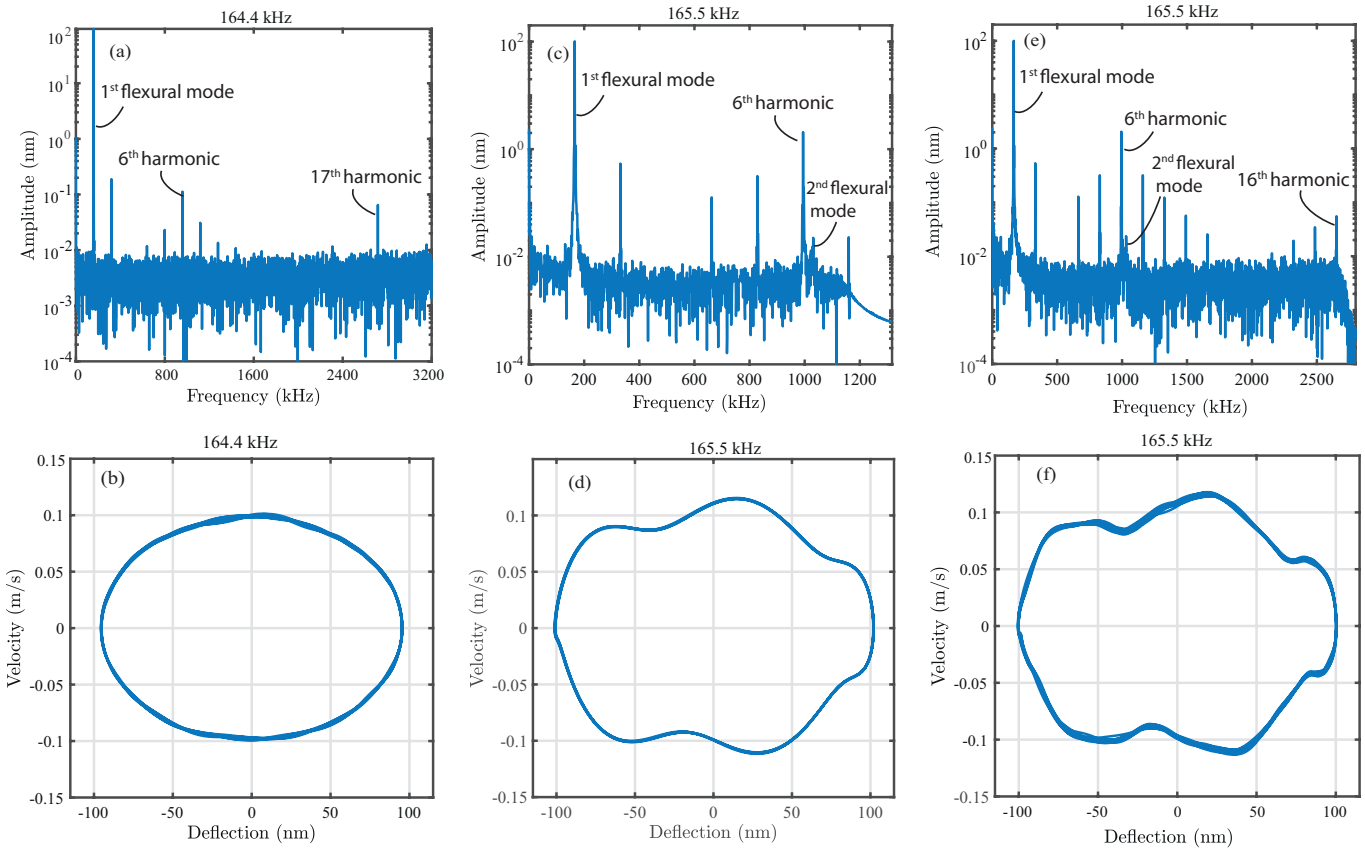

FIG. A.1: Influence of harmonics and higher order eigenmodes on phase space trajectories. (a)-(b) Discrete frequency spectra and the associated phase space trajectory at f_d = 164.4 kHz. (c)-(d) Discrete frequency spectra and the associated phase space trajectory at f_d = 165.5 kHz. The time data is low pass filtered to include the first 7 harmonics of the cantilever. (e)-(f) Discrete frequency spectra and the associated phase space trajectory at f_d = 165.5 kHz. The time data is low pass filtered to include the first 16 harmonics of the cantilever.

gradual warping of the phase space with characteristic ripples appearing on its periphery (see Fig. A.1(d)). Furthermore, by including the spectral components up to the 16^{th} harmonic (see Fig. A.1(e)), we see that the shape of the phase space trajectory is unaltered (see Fig. A.1(f)). However, if the time data at this particular frequency point was not low pass filtered then it would have resembled the phase space shown in Fig. 4. This analysis shows the insensitivity of the phase space trajectories to higher harmonics and further highlights the utility of phase space orbits as tools for probing the presence of higher order eigenmodes and modal interactions in dynamic AFM applications.

Appendix B: Theoretical model

Here, we obtain the dynamical equation for the AFM initially resting in a static equilibrium at a distance η^* from the sample (see Fig. B.1). The mathematical framework to develop the continuous model for the AFM cantilever is within the Euler-Bernoulli beam theory assumptions. The AFM cantilever has length L, mass density ρ, Young's modulus E, area moment of inertia I , and cross-section area A. The beam is clamped at $x = 0$ and free at $x = L$. The cantilever deflection is expressed in a non-inertial reference frame attached to the base, and excited with harmonic motion $y(t) = Y sin(\Omega t)$ via a dither piezo, where Y and Ω are the amplitude and frequency of excitation, respectively. The static deflection due to tip-sample forces at η^* is given by $w^*(x)$ (see Fig. B.1(a)). Finally, the instantaneous tip-sample distance is $z(t) = \eta^* - u(L,t) - y(t)$ where $u(x,t)$ is the dynamic deflection of the cantilever as shown in Fig. B.1(b). The vibrations about the elastostatic equilibrium are governed by the equation [23]:

$$\rho A\ddot{u}(x,t) + EI(u''''(x,t) + w^{*''''}(x)) = F_{ts}(z(t))\delta(x-L) + \rho A\Omega^2 Y sin(\Omega t). \tag{B1}$$

We discretize Eq. (B1) by projecting it onto linear mode shapes $\phi_i(x)$ computed around the cantilever static configuration. For this, we approximate the response as

$$u(x,t) = \sum_{i=1}^{n} \phi_i(x) q_i(t) \tag{B2}$$

with $q_i(t)$ being the generalized time dependent coordinate

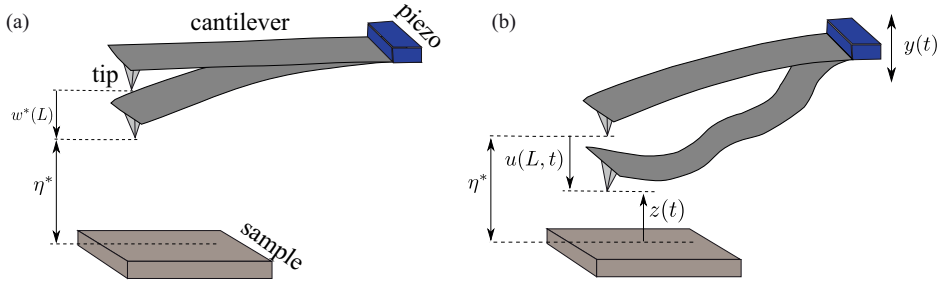

FIG. B.1: A schematic of the AFM. (a) Initially statically deflected configuration. (b) Dynamic configuration with the cantilever vibrating about its elastostatic equilibrium.

for the i-th mode of vibration. We then substitute Eq. (B2) in Eq. (B1) and by utilizing the Galerkin procedure we take the inner products with the same shape functions employed in the discretization. The final discretized dimensionless set of nonlinear ordinary differential equations are:

$$\ddot{\tilde{q}}_i + D_i(\bar{z})\dot{\tilde{q}}_i + K_i\tilde{q}_i = -C_i - F_{ts,i}(\bar{z}) + B_i\bar{\Omega}^2\bar{y}\sin\left(\bar{\Omega}\tau\right). \quad \text{(B3)}$$

where $\bar{z}$ is the dimensionless tip-sample separation distance given by

$$\bar{z} = 1 - \sum_{i=1}^{n}\tilde{q}_i - \bar{y}\sin\bar{\Omega}\tau. \quad \text{(B4)}$$

Replacing Eq. (B4) in the tip-sample interaction force (Eq. (1)) obtains

$$F_{ts,i}(\bar{z}) = \begin{cases} C_i/\bar{z}^2, & \text{for} \quad \bar{z} > \bar{a}_0 \\ C_i/\bar{a}_0^2 + G_i(\bar{a}_0 - \bar{z})^{3/2}, & \text{for} \quad \bar{z} \le \bar{a}_0. \end{cases} \quad \text{(B5)}$$

where the coefficients arising in Eqs. (B3),(B5) are defined as

$$K_i = \frac{{\omega_i}^2}{{\omega_0}^2}, \quad C_i = -\frac{HR{\phi_i}^2(L)}{6\rho A{\eta^*}^3{\omega_0}^2\int_0^L{\phi_i}^2(x)\,dx},$$
$$B_i = \frac{\phi_i(L)\int_0^L\phi_i(x)\,dx}{\int_0^L{\phi_i}^2(x)\,dx}, \quad G_i = \frac{4E^*\sqrt{R\eta^*}{\phi_i}^2(L)}{3\rho A{\omega_0}^2\int_0^L{\phi_i}^2(x)\,dx}. \quad \text{(B6)}$$

In the presented formulation the generalized coordinates $\tilde{q}_i$ are normalized with respect to the value of the mode shape at the free end of the cantilever ($\tilde{q}_i = \phi_i(L)\,q_i$). The overdot in Eq. (B3) means differentiation with respect to the dimensionless time, namely $\tau = \omega_0 t$ where ω_0 is the fundamental frequency of the cantilever. The amplitude and frequency of the excitation, Y and Ω are related to their dimensionless counterparts through $\bar{y} = Y/\eta^*$ and $\bar{\Omega} = \Omega/\omega_0$, respectively. Finally, $\bar{a}_0 = a_0/\eta^*$ is the dimensionless conjugate of the intermolecular distance a_0. Note that the modal damping $D_i(\bar{z})$ has been considered in Eq. (B3). Similar to Ref. [23], we consider a piecewise model that accounts for the dissipation mechanisms while the tip is in air ($\tilde{D}_i^{\text{att}}$) or in contact with the sample ($\tilde{D}_i^{\text{rep}}$):

$$D_i(\bar{z}) = \begin{cases} {D_i}^{\text{att}} = \dfrac{\tilde{D}_i^{\text{att}}}{\omega_0\rho A\int_0^L{\phi_i}^2(x)\,dx}, & \text{for} \quad \bar{z} > \bar{a}_0 \\ {D_i}^{\text{rep}} = \dfrac{\tilde{D}_i^{\text{rep}}}{\omega_0\rho A\int_0^L{\phi_i}^2(x)\,dx}, & \text{for} \quad \bar{z} \le \bar{a}_0. \end{cases} \quad \text{(B7)}$$

In our simulations we restrict ourselves to a two-degree-of-freedom model, that means we limit Eq.(B3) to $i = 2$. In this case the coupled set of nonlinear differential equations become:

$$\begin{cases} \ddot{\tilde{q}}_1 + D_1^{\text{att}}\dot{\tilde{q}}_1 + K_1\tilde{q}_1 = -C_1 - \dfrac{C_1}{\left(1-\tilde{q}_1-\tilde{q}_2-\bar{y}\sin\bar{\Omega}\tau\right)^2} \\ \qquad\qquad + B_1\bar{\Omega}^2\bar{y}\sin\left(\bar{\Omega}\tau\right) \\ \ddot{\tilde{q}}_2 + D_2^{\text{att}}\dot{\tilde{q}}_2 + K_2\tilde{q}_2 = -C_2 - \dfrac{C_2}{\left(1-\tilde{q}_1-\tilde{q}_2-\bar{y}\sin\bar{\Omega}\tau\right)^2} \\ \qquad\qquad + B_2\bar{\Omega}^2\bar{y}\sin\left(\bar{\Omega}\tau\right) \end{cases}. \quad \text{(B8)}$$

$$\begin{cases} \ddot{\tilde{q}}_1 + D_1^{\text{rep}}\dot{\tilde{q}}_1 + K_1\tilde{q}_1 = -C_1 - C_1/\bar{a}_0^2 \\ -G_1\left(\bar{a}_0 - \left(1-\tilde{q}_1-\tilde{q}_2-\bar{y}\sin\bar{\Omega}\tau\right)\right)^{3/2} + B_1\bar{\Omega}^2\bar{y}\sin\left(\bar{\Omega}\tau\right) \\ \ddot{\tilde{q}}_2 + D_2^{\text{rep}}\dot{\tilde{q}}_2 + K_2\tilde{q}_2 = -C_2 - C_2/\bar{a}_0^2 \\ -G_2\left(\bar{a}_0 - \left(1-\tilde{q}_1-\tilde{q}_2-\bar{y}\sin\bar{\Omega}\tau\right)\right)^{3/2} + B_2\bar{\Omega}^2\bar{y}\sin\left(\bar{\Omega}\tau\right) \end{cases}. \quad \text{(B9)}$$

where Eq.(B8) and (B9) shall be integrated with conditions $\left(1-\tilde{q}_1-\tilde{q}_2-\bar{y}\sin\bar{\Omega}\tau\right) \le \bar{a}_0$ and $\left(1-\tilde{q}_1-\tilde{q}_2-\bar{y}\sin\bar{\Omega}\tau\right) > \bar{a}_0$, respectively.

The simulation parameters used in Eq.(B8) and (B9) to obtain the results presented in Fig.3 are provided in the supplementary information S2.

Appendix C: Phase synchronization at internal resonance

We reported a reduction in sample indentation in Fig. 2(a) when f_d is detuned to coincide with the sweet spot. In this appendix, we utilize the simulations from our two mode VdW-DMT model described in Eq. (B9) and show that the phase synchronization between the eigenmodes is responsible for the aforementioned reduction in sample indentation. Figure. C.1 shows the time signals of the first (blue) and second (orange) flexural modes extracted from the same simulations reported in Fig. 3. The signals are extracted at different excitation frequencies from the nonlinear frequency response curve to track the variation of phase difference between the two modes. At resonance $f_d = f_0$ (see Fig. C.1(a)) the phase difference between the two modes is $\approx 90°$. However, when f_d is detued to enter the sweet spot (see Fig. C.1(b)-(c)), the phase difference changes drastically such that the two modes interact almost in out-of-phase motion. The phase difference between the two modes is found to be $152.11°$ to $163.38°$ as f_d is swept from 165.5 kHz to 166 kHz, respectively. This out-of-phase motion between the two eigenmodes interfere destructively, resulting in a reduced sample indentation. Finally, when f_d is out of the sweet spot range the phase difference gradually shrinks to $32.4°$ at 167 kHz (see Fig. C.1(d)). This reduction in phase difference causes the two modes to interfere constructively and therefore results in larger indentation at higher excitation frequencies.

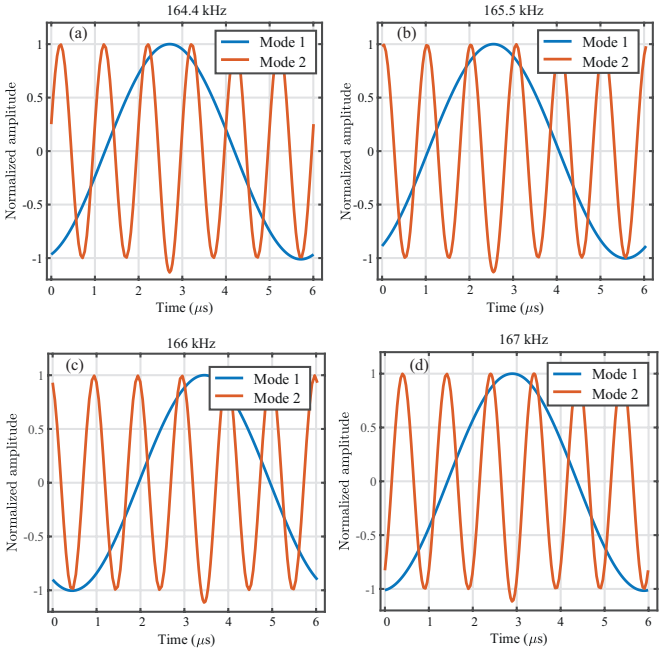

FIG. C.1: Simulations depicting Auto phase synchronization between first (blue) and second (orange) flexural modes in the sweet spot. To aid with the visualization, the amplitudes of the time signals are normalized with respect to their corresponding maximum value in a given time period. (a) At resonance, the first and second flexural mode oscillations start with a phase difference of $90°$ (b)-(c) The phase difference between the two eigenmodes in the sweet spot at 165.5 kHz and 166 kHz, respectively.(d) the phase difference between the two modes out of the sweet spot at 167 kHz.

[1] Y. F. Dufrêne, T. Ando, R. Garcia, D. Alsteens, D. Martinez-Martin, A. Engel, C. Gerber, and D. J. Müller, Imaging modes of atomic force microscopy for application in molecular and cell biology, Nature Nanotechnology **12**, 295 (2017).

[2] R. Garcia and E. T. Herruzo, The emergence of multifrequency force microscopy, Nature nanotechnology **7**, 217 (2012).

[3] R. Hillenbrand, M. Stark, and R. Guckenberger, Higher-harmonics generation in tapping-mode atomic-force microscopy: Insights into the tip–sample interaction, Applied Physics Letters **76**, 3478 (2000).

[4] M. Stark, R. W. Stark, W. M. Heckl, and R. Guckenberger, Spectroscopy of the anharmonic cantilever oscillations in tapping-mode atomic-force microscopy, Applied Physics Letters **77**, 3293 (2000).

[5] E. T. Herruzo, A. P. Perrino, and R. Garcia, Fast nanomechanical spectroscopy of soft matter, Nature communications **5**, 1 (2014).

[6] D. Martinez-Martin, E. T. Herruzo, C. Dietz, J. Gomez-Herrero, and R. Garcia, Noninvasive protein structural flexibility mapping by bimodal dynamic force microscopy, Phys. Rev. Lett. **106**, 198101 (2011).

[7] O. Sahin, Time-varying tip-sample force measurements and steady-state dynamics in tapping-mode atomic force microscopy, Physical Review B **77**, 115405 (2008).

[8] D. Platz, E. A. Tholén, D. Pesen, and D. B. Haviland, Intermodulation atomic force microscopy, Applied Physics Letters **92**, 153106 (2008).

[9] R. Garcia and R. Proksch, Nanomechanical mapping of soft matter by bimodal force microscopy, European Polymer Journal **49**, 1897 (2013).

[10] P.-A. Thorén, R. Borgani, D. Forchheimer, I. Dobryden, P. M. Claesson, H. G. Kassa, P. Leclère, Y. Wang, H. M. Jaeger, and D. B. Haviland, Modeling and measuring viscoelasticity with dynamic atomic force microscopy, Physical Review Applied **10**, 024017 (2018).

[11] A. Raman, S. Trigueros, A. Cartagena, A. P. Stevenson, M. Susilo, E. Nauman, and S. A. Contera, Mapping nanomechanical properties of live cells using multi-harmonic atomic force microscopy, Nat Nanotechnol **6**, 809 (2011).

[12] M. Dong, S. Husale, and O. Sahin, Determination of protein structural flexibility by microsecond force spectroscopy, Nature nanotechnology **4**, 514 (2009).

[13] O. Sahin, Time-varying tip-sample force measurements and steady-state dynamics in tapping-mode atomic force microscopy, Physical Review B **77**, 115405 (2008).

[14] R. Potekin, S. Dharmasena, D. M. McFarland, L. A. Bergman, A. F. Vakakis, and H. Cho, Cantilever dynamics in higher-harmonic atomic force microscopy for enhanced material characterization, International Journal of Solids and Structures **110-111**, 332 (2017).

[15] A. Keyvani, H. Sadeghian, M. S. Tamer, J. F. L. Goosen, and F. van Keulen, Minimizing tip-sample forces and enhancing sensitivity in atomic force microscopy with dynamically compliant cantilevers, Journal of Applied Physics **121**, 244505 (2017).

[16] O. Sahin, G. Yaralioglu, R. Grow, S. F. Zappe, A. Atalar, C. Quate, and O. Solgaard, High-resolution imaging of elastic properties using harmonic cantilevers, Sensors and Actuators A: Physical **114**, 183 (2004).

[17] H. Li, Y. Chen, and L. Dai, Concentrated-mass cantilever enhances multiple harmonics in tapping-mode atomic force microscopy, Applied Physics Letters **92**, 151903 (2008).

[18] A. H. Nayfeh and D. T. Mook, *Nonlinear oscillations* (John Wiley & Sons, 2008).

[19] Ata Keskekler, Oriel Shoshani, Martin Lee, Herre S. J. van der Zant, Peter G. Steeneken, and Farbod Alijani. Enhancing nonlinear damping by parametric-direct internal resonance, 2020.

[20] J. E. Sader, J. W. M. Chon, and P. Mulvaney, Calibration of rectangular atomic force microscope cantilevers, Review of Scientific Instruments **70**, 3967 (1999).

[21] E. Rull Trinidad, T. Gribnau, P. Belardinelli, U. Staufer, and F. Alijani, Nonlinear dynamics for estimating the tip radius in atomic force microscopy, Applied Physics Letters **111**, 123105 (2017).

[22] A. Chandrashekar, P. Belardinelli, U. Staufer, and F. Alijani, Robustness of attractors in tapping mode atomic force microscopy, Nonlinear Dynamics **97**, 1137 (2019).

[23] S. I. Lee, S. W. Howell, A. Raman, and R. Reifenberger, Nonlinear dynamic perspectives on dynamic force microscopy, Ultramicroscopy **97**, 185 (2003).

[24] R. García and A. San Paulo, Attractive and repulsive tip-sample interaction regimes in tapping-mode atomic force microscopy, Phys. Rev. B **60**, 4961 (1999).

[25] H. Dankowicz and F. Schilder, *Recipes for Continuation*, Computational Science and Engineering (Society for Industrial and Applied Mathematics, 2013).

[26] Andrew N Round and Mervyn J Miles. Exploring the consequences of attractive and repulsive interaction regimes in tapping mode atomic force microscopy of DNA. Nanotechnology, 15 (2004).

[27] Robert W. Stark. Bistability, higher harmonics, and chaos in AFM. Materials Today, 13 (2010).

[28] Hendrik Holscher and Udo D. Schwarz. Theory of amplitude modulation atomic force microscopy with and without q-control. *International Journal of Non-Linear Mechanics*, 42(4):608 – 625, 2007. Special Issue Micro-and Nanoscale Beam Dynamics.

[29] Ilham Kirrou and Mohamed Belhaq. Control of bistability in non-contact mode atomic force microscopy using modulated time delay. *Nonlinear Dynamics*, 81(1):607–619, 2015.